Deterministic quantum teleportation with feed-forward in a solid state system

— Source link ↗

L. Steffen, Yves Salathé, M. Oppliger, Philipp Kurpiers ...+8 more authors

Institutions: ETH Zurich, University of Queensland

Topics: Quantum teleportation, Quantum network, Quantum error correction, Quantum channel and Quantum information

Related papers:

- Teleporting an unknown quantum state via dual classical and Einstein-Podolsky-Rosen channels

- Experimental quantum teleportation

- Deterministic quantum teleportation of atomic qubits.

- Deterministic quantum teleportation with atoms

- Cavity quantum electrodynamics for superconducting electrical circuits: An architecture for quantum computation

LETTER

Deterministic quantum teleportation with feed–forward in a solid state system

L. Steffen[1], Y. Salathe[1], M. Oppliger[1], P. Kurpiers[1], M. Baur[1]†, C. Lang[1], C. Eichler[1], G. Puebla–Hellmann[1], A. Fedorov[1]† & A. Wallraff[1]

Engineered macroscopic quantum systems based on superconducting electronic circuits are attractive for experimentally exploring diverse questions in quantum information science[1–3]. At the current state of the art, quantum bits (qubits) are fabricated, initialized, controlled, read out and coupled to each other in simple circuits. This enables the realization of basic logic gates[4], the creation of complex entangled states[5,6] and the demonstration of algorithms[7] or error correction[8]. Using different variants of low-noise parametric amplifiers[9], dispersive quantum non-demolition single-shot readout of single-qubit states with high fidelity has enabled continuous[10] and discrete[11] feedback control of single qubits. Here we realize full deterministic quantum teleportation with feed-forward in a chip-based superconducting circuit architecture[12–14]. We use a set of two parametric amplifiers for both joint two-qubit and individual qubit single-shot readout, combined with flexible real-time digital electronics. Our device uses a crossed quantum bus technology that allows us to create complex networks with arbitrary connecting topology in a planar architecture. The deterministic teleportation process succeeds with order unit probability for any input state, as we prepare maximally entangled two-qubit states as a resource and distinguish all Bell states in a single two-qubit measurement with high efficiency and high fidelity. We teleport quantum states between two macroscopic systems separated by 6 mm at a rate of $10^4\,\mathrm{s}^{-1}$, exceeding other reported implementations. The low transmission loss of superconducting waveguides is likely to enable the range of this and other schemes to be extended to significantly larger distances, enabling tests of non-locality and the realization of elements for quantum communication at microwave frequencies. The demonstrated feed-forward may also find application in error correction schemes.

Transferring the state of an information carrier from a sender to a receiver is an essential primitive in both classical and quantum communication and information processing. In a quantum mechanical context, teleportation describes the process of transferring an unknown quantum state between two parties at two different physical locations without transferring the physical carrier of information itself. Instead, teleportation makes use of the non-local correlations provided by an entangled pair shared between the sender and the receiver and the exchange of classical information[15]. This concept is central to extending the range of quantum communication using quantum repeaters[16] and can also be used to implement logic gates for universal quantum computation[17].

In the original teleportation protocol[15], the unknown state $|\psi_{\mathrm{in}}\rangle$ of qubit Q1 in possession of the sender is transferred to the receiver's qubit, Q3 (Fig. 1a). To enable this task, sender and receiver prepare in advance a maximally entangled (Bell) state between an ancillary qubit Q2, which remains with the sender, and Q3, which is located at the receiver. Then the sender performs a measurement of Q1 and Q2 in the Bell basis, which projects the two qubits in the sender's possession onto one of the four possible Bell states $|\Phi^{\pm}\rangle = (|00\rangle \pm |11\rangle)/\sqrt{2}$ and $|\Psi^{\pm}\rangle = (|01\rangle \pm |10\rangle)/\sqrt{2}$. As a consequence the receiver's qubit Q3 is projected instantaneously and without ever having interacted with the sender's qubit Q1 onto a state $|\psi_{\mathrm{out}}\rangle = \{\mathbb{1}, X, Z, \tilde{Y}\}\,|\psi_{\mathrm{in}}\rangle$ (where

$X = \hat{\sigma}_x$, $Z = \hat{\sigma}_z$ and $\tilde{Y} = i\hat{\sigma}_y$ are the Pauli matrices), which differs from the input state $|\psi_{\mathrm{in}}\rangle$ only by a single-qubit rotation, depending on the four possible measurement results. To always recover the original state $|\psi_{\mathrm{in}}\rangle$ the receiver has to rotate the output state of Q3 conditioned on the outcome of the Bell measurement communicated to the receiver as two bits of information by means of a classical channel. This final step is frequently referred to as feed-forward, because the outcome of a measurement performed on one part of a system is used to control another part of the same quantum system. This is in contrast to acting back on the same quantum system in a feedback process.

The success of the teleportation protocol in every instance with unit fidelity is counterintuitive from a classical point of view. The receiver's qubit does not interact with any other qubit after $|\psi_{\mathrm{in}}\rangle$ is prepared. The classical information sent by the sender is not sufficient to recreate $|\psi_{\mathrm{in}}\rangle$ perfectly at the receiver. Indeed, assuming no entanglement between sender and receiver, one can replicate the sender's state at best with a fidelity of 2/3 (ref. 18) because only a fraction of information about $|\psi_{\mathrm{in}}\rangle$ is obtained by a single projective measurement.
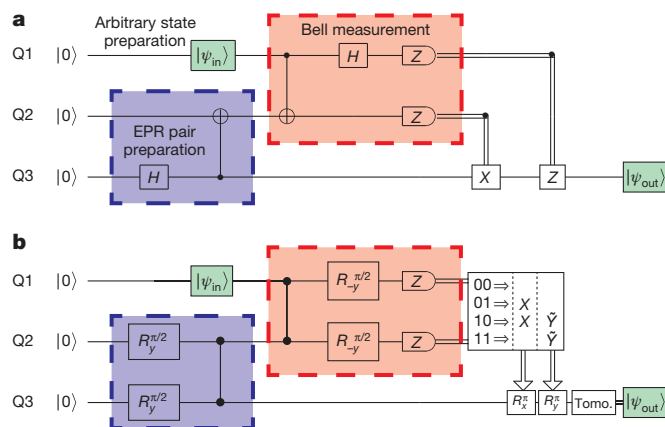

Figure 1 | Circuit diagram of quantum teleportation. a, The original protocol starts with the preparation of a Bell state between Q2 and Q3 (blue box), followed by the preparation of an arbitrary state $|\psi_{\mathrm{in}}\rangle$ (green box) and a Bell-state measurement of Q1 and Q2 (red box). The classical information extracted by the measurement of Q1 and Q2 is transferred to the receiver to perform local gates conditioned on the measurement outcomes. After the protocol, Q3 is in state $|\psi_{\mathrm{out}}\rangle$, which ideally is identical to $|\psi_{\mathrm{in}}\rangle$ (also coloured green). Here, H is the Hadamard gate, and X and Z are Pauli matrices. The CNOT gate is represented by a vertical line between the control qubit ($\bullet$) and the target qubit ($\oplus$). **b,** The protocol implemented in our experiment uses controlled-PHASE gates indicated by vertical lines between the relevant qubits ($\bullet$), and single-qubit rotations $R_{\pm y}^{\theta}$ of angle θ about the $\pm y$ axis. To finalize the teleportation we either post-select on any single one of the four measurement outcomes (00, 01, 10 and 11) acquired in a single shot, or we deterministically use all four outcomes, which we then may use to implement feed-forward. The feed-forward operators R_x^{π} and R_y^{π} are applied to Q3 conditioned on the four measurement outcomes according to the table presented in the box framed by a black line.

[1]Department of Physics, ETH Zurich, CH-8093 Zurich, Switzerland. †Present address: ARC Centre for Engineered Quantum Systems, University of Queensland, Brisbane 4072, Australia.

In pioneering work the teleportation protocol was first implemented with single photons[19] over laboratory-scale distances and later also over kilometre-scale distances in free space[20]. However, in these experiments only two out of four Bell states were distinguished unambiguously, limiting the efficiency of the protocol to 50% at best. A proof-of-principle experiment that can distinguish all four Bell states was implemented using nonlinear photon interaction[21], but the efficiency of the detection step was much below 1%. With photonic continuous-variable states, teleportation has been achieved deterministically for all measurement outcomes and the final conditional rotation has been implemented to complete the teleportation protocol[22]. In atomic qubits, fully deterministic quantum teleportation has been realized over micrometre-scale distances with ions in the same trap[23,24]. Non-deterministically the protocol has also been implemented between ions in different traps[25] and in atomic ensembles[26].

The experimental realization of teleportation faces several important challenges that have been sequentially addressed over many years of research in most physical realizations. The ideal protocol requires the creation of an entangled pair shared between the sender and the receiver, a two-qubit measurement identifying all four Bell states at the sender, and feed-forward of the classical information to perform the final qubit state rotation to complete the protocol, all at high efficiency and fidelity. In addition it is frequently desired to run the protocol at a high rate and over large distances to maximize its usefulness.

Here we demonstrate in a solid state system post-selected teleportation, deterministic teleportation and deterministic teleportation with feed-forward in a single experimental setting. Our experiment addresses all of the above criteria with the exception of realizing space-like separation between the sender and the receiver. The coherent part of the teleportation protocol presented here has previously been characterized

in our laboratory by performing full-state tomography of three qubits interacting with a single mode field[27]. That work has allowed us to test the protocol up to, but not including, the essential single-shot readout and feed-forward steps, which are the focus of this study.

In the realization of teleportation presented here, we use three super-conducting transmon qubits[3] (Q1, Q2 and Q3) coupled to three super-conducting coplanar waveguide resonators (R1, R2 and R3) in a circuit quantum electrodynamics setup[12] (Fig. 2). At the sender, qubits Q1 and Q2 are coupled capacitively to resonator R1; at the receiver, Q3 is coupled to R3. The individual resonators R1 and R3 allow the sender and the receiver to perform independent measurements of their qubits, as detailed below. In addition, Q2 and Q3 are coupled to R2. The resonators R2 and R1 act as quantum buses to realize two-qubit controlled-PHASE (CPHASE) gates[7] used to create a shared Bell state distributed between the sender and the receiver and to perform a deterministic Bell state analysis at the sender. We perform single-qubit rotations with an average fidelity of greater than 98% by applying amplitude-controlled and phase-controlled microwave pulses through individual charge gate lines. The transition frequency of each qubit is controlled by individual flux bias lines.

We start the protocol by heralding the three-qubit ground state based on a single-shot measurement of all qubits. Using single-qubit rotations and a CPHASE gate with process fidelity 90%, a Bell state with state fidelity 92% is created on demand between qubits Q2 and Q3 that is shared between the sender and the receiver (blue box in Fig. 1b). Only after the creation of the shared entanglement, we use a single-qubit rotation to prepare the state of qubit Q1 to be teleported.

As an essential part of the protocol, we perform a Bell measurement of qubits Q1 and Q2 at the sender by mapping the Bell basis $\{|\Phi^-\rangle, |\Psi^-\rangle, |\Phi^+\rangle, |\Psi^+\rangle\}$ onto the computational basis $\{|00\rangle, |01\rangle, |10\rangle, |11\rangle\}$ using a CNOT gate and a Hadamard gate (red box in
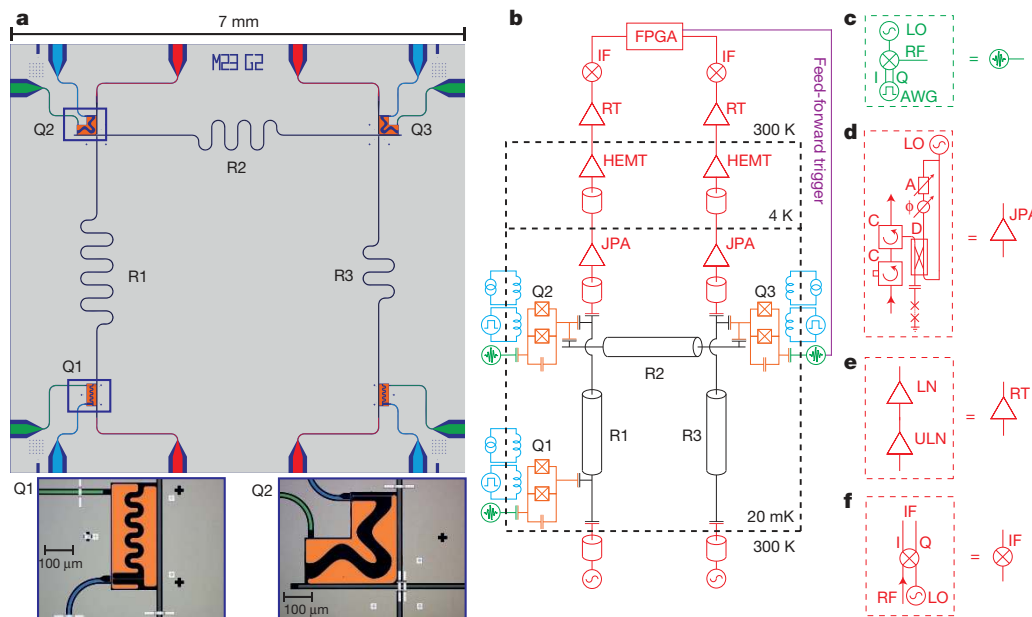

Figure 2 | Diagrams of sample and measurement setup. a, Chip design including three resonators R1, R2 and R3 (black) with corresponding input and output lines (red) used for readout and coupling of three transmon qubits Q1, Q2 and Q3 (orange). The fourth qubit in the lower right corner of the chip is not used. The local microwave charge gate lines (green) are used for single-qubit rotations; the local flux-bias lines (blue) permit nanosecond time control of the qubit frequencies to implement two-qubit operations. Below: false-colour micrographs of Q1 (left) coupled to resonator R1, and Q2 (right) coupled to both resonators R1 and R2. The microfabricated aluminium air bridges visible as bright white strips realize crossovers for the resonator lines. Air bridges are also used to suppress spurious electromagnetic modes by connecting the ground planes across the coplanar wave guides. **b**, Simplified diagram of the measurement setup with the same colour code as in **a**. **c**, Amplitude-controlled and phase-controlled microwave pulses are applied to the qubits using

sideband modulation of an up-conversion in-phase quadrature (IQ) mixer driven by a local oscillator (LO) and modulated by an arbitrary waveform generator (AWG). **d**, The measurement signals transmitted through R1 and R3 are amplified using Josephson parametric amplifiers (JPA) pumped by an LO through a directional coupler (D), which is also used for phase (ϕ) and amplitude (A) controlled cancellation of the pump leakage, and coupled to and isolated from the sample by two circulators (C). **e**, The signal is further amplified by high-electron-mobility transistor (HEMT) amplifiers at 4 K and chains of ultra-low-noise (ULN) and low-noise (LN) room-temperature (RT) amplifiers. **f**, The transmission signal of both resonators is down-converted to an intermediate frequency (IF) in an IQ mixer pumped by a dedicated LO, digitized, and fed into field-programmable gate array (FPGA) logic for real-time data analysis and triggering the conditioned feed-forward step.

Fig. 1a). We realize this basis transformation by using single-qubit rotations and a CPHASE gate. Then we perform a projective joint readout[28] of the states of Q1 and Q2 by measuring the transmission amplitude and phase of resonator R1. A given Bell state is transformed to the corresponding computational basis state, resulting in the corresponding output state $|\psi_{out}\rangle = \{\mathbb{1}, X, Z, \tilde{Y}\} |\psi_{in}\rangle$ of Q3.

To perform a post-selected teleportation protocol, it is sufficient to distinguish only one of the four Bell states, say $|00\rangle$, ideally occurring with a probability of 1/4, with high fidelity from all other states ($|01\rangle$, $|10\rangle$ and $|11\rangle$) by using the aforementioned scheme. This is possible in our setup by performing a dispersive single-shot qubit readout with a fidelity of $(91.0 \pm 0.2)\%$. For this purpose we amplify a measurement tone applied to R1 with a Josephson parametric amplifier operated in the phase-sensitive mode, in which no or only very little noise is added to the signal[9]. If the measurement of Q1 and Q2 returns 00, qubit Q3 is instantaneously projected to the desired state $|\psi_{in}\rangle$ not requiring any additional rotations at the receiver's qubit to complete teleportation.

With a second, independent, parametric amplifier, also operated in the phase-sensitive mode, a measurement tone transmitted through resonator R3 is used to read out the state of qubit Q3 with a single-shot fidelity of $(89.1 \pm 0.5)\%$. In post-selection (ps), state tomography of Q3 conditioned on a 00 measurement of Q1 and Q2 reveals the original input state with an average fidelity of $\bar{\mathcal{F}}_s^{ps,00} = (81.9 \pm 1.3)\%$ (Extended Data Fig. 3a). By characterizing $|\psi_{out}\rangle$ for four linearly independent input states $|\psi_{in}\rangle$, we perform full process tomography[29] of the state transfer by teleportation from Q1 to Q3 to reconstruct the process matrix χ_{00}, which has a fidelity of $\mathcal{F}_p^{ps,00} = (72.5 \pm 1.3)\%$ with respect to the expected identity operation. The process fidelity $\mathcal{F}_p$ is related to the average output-state fidelity $\bar{\mathcal{F}}_s$ by $\mathcal{F}_p = (\bar{\mathcal{F}}_s(d+1) - 1)/d$, where d is the dimensionality of the input state and output state.

It is important to note that in post-selection we are able to map any of the four Bell states to the computational basis state $|00\rangle$ on demand by applying π-pulses to Q1 and/or Q2 right before their joint readout. This allows us to post-select individually on any of the four Bell states and to determine the corresponding process matrices $\chi_{00,01,10,11}$. The experimentally obtained process matrices (Fig. 3a) agree well with the expected processes. The average output-state fidelity $\bar{\mathcal{F}}_s^{ps} = (81.7 \pm 1.4)\%$ of all four processes is clearly above the classical limit of 2/3 (ref. 18). This results in an average process fidelity when post-selecting on a single Bell state of $\bar{\mathcal{F}}_p^{ps} = (72.0 \pm 1.4)\%$, well above the classical limit of 1/2. The output-state fidelity is predominantly limited by the relaxation and dephasing of our qubits, which affects both the effective gate and readout fidelity (see Methods).

To identify uniquely and simultaneously the four randomly distributed outcomes of the Bell-state measurement at the sender in a deterministic way (instead of using post-selection) we use high-fidelity dispersive single-shot qubit readout enabled by the Josephson parametric amplifier operated in the phase-preserving mode[30]. In this mode we achieve a probability of $(81.8 \pm 0.5)\%$ to correctly identify all four pairs of basis states, by amplifying and recording both quadrature amplitudes (I, Q) of the detected electromagnetic field at the cost of adding at least the vacuum noise to the input signal. Correlating the four single-shot Bell-state measurement outcomes at the sender with the single-shot measurement outcomes at the receiver, and performing state and process tomography, we find an average deterministic output-state fidelity of the transferred state of $\bar{\mathcal{F}}_s^{det} = (77.1 \pm 1.2)\%$ and an average process fidelity of $\bar{\mathcal{F}}_p^{det} = (65.5 \pm 1.1)\%$, well above the classical limits of 2/3 and 1/2, respectively. The process matrices (Fig. 3b) prominently show the characteristic features of the expected processes. The fidelities obtained with this method are lower than for the post-selected teleportation, because of the lower fidelity of the deterministic Bell-state readout.
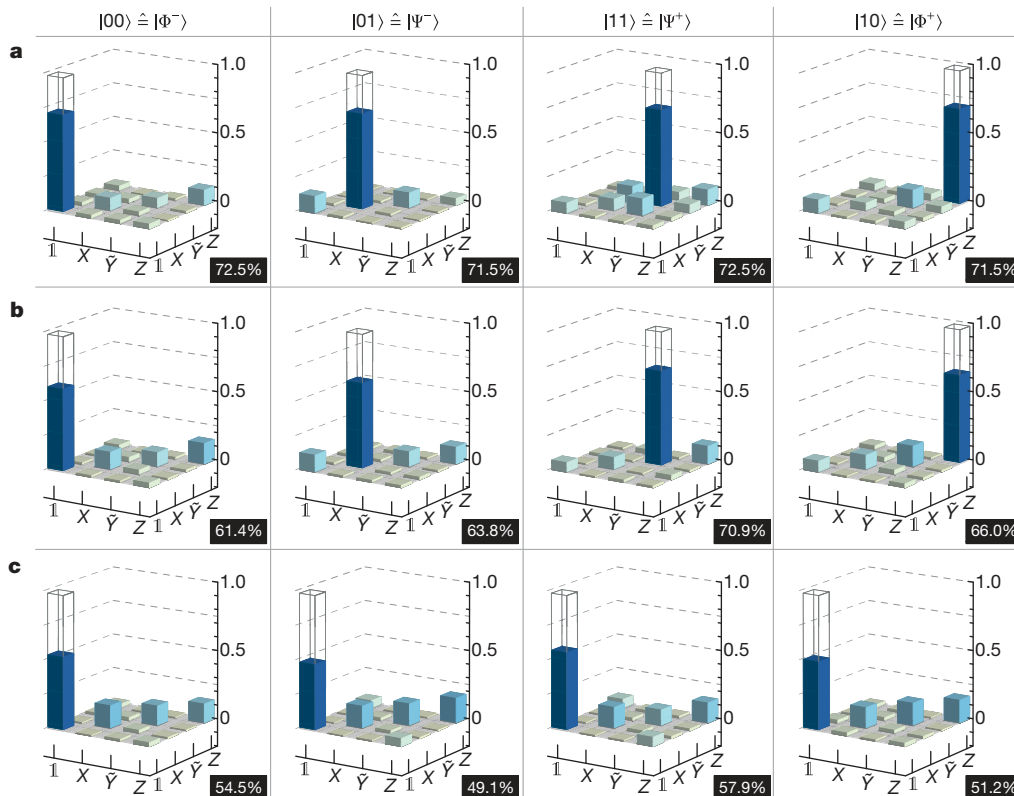

Figure 3 | State-transfer process matrix for quantum teleportation. The experimentally obtained (solid bars) absolute values of the process matrices $|\chi|$ describing the state transfer from Q1 to Q3 by teleportation are displayed for post-selection on any single one of the Bell-measurement outcomes 00, 01, 10 and 11 (**a**), simultaneous deterministic measurement of all four outcomes (**b**), and with feed-forward (**c**). The respective process fidelities are indicated in black boxes. The ideal $|\chi|$ is indicated by wire frames.

To complete the teleportation protocol we have analysed the deterministic Bell-state measurement in real time by using fast electronics based on a field programmable gate array (FPGA). Digitally defining two thresholds for the single-shot measurements of the quadrature amplitudes I and Q performed at the sender we realize the feed-forward (ff) step in about 500 ns, in which the rotations $I, X, \tilde{Y}X (= Z), \tilde{Y}$ are applied conditioned on the four Bell-state measurement outcomes 00, 01, 10 and 11. We analysed more than 270,000 single-shot experiments and find a deterministic state-transfer fidelity of $\bar{\mathcal{F}}_s^{ff} = (68.8 \pm 0.5)\%$ with a process fidelity $\mathcal{F}_p^{ff} = (53.2 \pm 0.5)\%$, close to but clearly above the classical thresholds (Fig. 3c). The limited fidelity can be traced back to the fidelities of single-qubit and two-qubit operations, the readout fidelities and the time required for the feed-forward in relation to the coherence times of the qubits used.

When averaging and appropriately normalizing the measurement results of Q3 directly in the FPGA, we are able to circumvent the limited single-shot readout fidelity of Q3. In this case, the deterministically teleported states including the feed-forward step have an average fidelity of $\bar{\mathcal{F}}_s^{av} = (77.4 \pm 0.2)\%$, with a corresponding process fidelity of $\mathcal{F}_p^{av} = (62.2 \pm 0.3)\%$.

To characterize the feed-forward process only, we have prepared separable input states ($|00\rangle, |01\rangle, |10\rangle$ and $|11\rangle$) of Q1 and Q2, and arbitrary states $|\psi\rangle$ of Q3. The input states measured and digitally analysed at the sender are then used to actuate the feed-forward. The fidelity of the resulting state of Q3 subject to feed-forward was determined to be $\bar{\mathcal{F}}_s = (79.5 \pm 1.5)\%$ with a corresponding process fidelity of $\mathcal{F}_p = (72.4 \pm 1.5)\%$. These results also indicate that this type of deterministic feed-forward can in principle be used for demonstrating error correction in future experiments, if high enough fidelities can be realized.

These results, in conjunction with continuing improvements in coherence time[3], advances in circuit design and operation, and the potential for using propagating microwave photons, form a solid ground for future progress in quantum information processing and quantum communication with superconducting circuits.

METHODS SUMMARY

The teleportation protocol (Fig. 1b) is implemented using the pulse scheme depicted in Extended Data Fig. 1. Single-qubit rotations are realized by 12 ns long resonant microwave pulses. Controlled-PHASE gates are implemented by shifting one of the two qubits' transition frequencies to the avoided level crossing between the $|11\rangle$ and $|02\rangle$ states. For single-shot measurements, the output signals of resonators R1 and R3 are amplified using Josephson parametric amplifiers. For the experiments in which we post-select on an individual Bell state, we operate the parametric amplifier in the phase-sensitive mode. This allows us to distinguish the state $|00\rangle$ from all other states by analysing the integrated measurement signal (Extended Data Fig. 2a). In the experiments in which we simultaneously distinguish between all four Bell states, the parametric amplifier is used in the phase-preserving mode, in which both quadratures of the transmitted field are amplified. By adjusting the pump and readout powers we maximize the distinguishability of all four states by their respective quadrature amplitudes in the complex plane (Extended Data Fig. 2b). To implement the feed-forward, all measurement data are analysed in real-time in an FPGA with custom firmware. Depending on the measurement outcome, the FPGA triggers up to two arbitrary waveform generators, which realize X and Y rotations. We characterize the state transfer from Q1 to Q3 with full process tomography by performing state tomography on the output state for four different linearly independent input states (Extended Data Fig. 3). We also use the teleportation protocol to verify the entanglement between Q2 and Q3 using six mutually unbiased input basis states.

Online Content Any additional Methods, Extended Data display items and Source Data are available in the online version of the paper; references unique to these sections appear only in the online paper.

1. Clarke, J. & Wilhelm, F. K. Superconducting quantum bits. *Nature* **453**, 1031–1042 (2008).
2. Houck, A. A., Tureci, H. E. & Koch, J. On-chip quantum simulation with superconducting circuits. *Nature Phys.* **8**, 292–299 (2012).
3. Devoret, M. & Schoelkopf, R. J. Superconducting circuits for quantum information: an outlook. *Science* **339**, 1169–1174 (2013).
4. Steffen, M. *et al.* Measurement of the entanglement of two superconducting qubits via state tomography. *Science* **313**, 1423–1425 (2006).
5. DiCarlo, L. *et al.* Preparation and measurement of three-qubit entanglement in a superconducting circuit. *Nature* **467**, 574–578 (2010).
6. Neeley, M. *et al.* Generation of three-qubit entangled states using superconducting phase qubits. *Nature* **467**, 570–573 (2010).
7. DiCarlo, L. *et al.* Demonstration of two-qubit algorithms with a superconducting quantum processor. *Nature* **460**, 240–244 (2009).
8. Reed, M. D. *et al.* Realization of three-qubit quantum error correction with superconducting circuits. *Nature* **482**, 382–385 (2012).
9. Castellanos-Beltran, M. A., Irwin, K. D., Hilton, G. C., Vale, L. R. & Lehnert, K. W. Amplification and squeezing of quantum noise with a tunable Josephson metamaterial. *Nature Phys.* **4**, 929–931 (2008).
10. Vijay, R. *et al.* Stabilizing Rabi oscillations in a superconducting qubit using quantum feedback. *Nature* **490**, 77–80 (2012).
11. Johnson, J. E. *et al.* Heralded state preparation in a superconducting qubit. *Phys. Rev. Lett.* **109**, 050506 (2012).
12. Wallraff, A. *et al.* Strong coupling of a single photon to a superconducting qubit using circuit quantum electrodynamics. *Nature* **431**, 162–167 (2004).
13. Helmer, F. *et al.* Cavity grid for scalable quantum computation with superconducting circuits. *Europhys. Lett.* **85**, 50007 (2009).
14. Mariantoni, M. *et al.* Implementing the quantum von Neumann architecture with superconducting circuits. *Science* **334**, 61–65 (2011).
15. Bennett, C. H. *et al.* Teleporting an unknown quantum state via dual classical and Einstein–Podolsky–Rosen channels. *Phys. Rev. Lett.* **70**, 1895–1899 (1993).
16. Gisin, N., Ribordy, G., Tittel, W. & Zbinden, H. Quantum cryptography. *Rev. Mod. Phys.* **74**, 145–195 (2002).
17. Gottesman, D. & Chuang, I. L. Demonstrating the viability of universal quantum computation using teleportation and single-qubit operations. *Nature* **402**, 390–393 (1999).
18. Massar, S. & Popescu, S. Optimal extraction of information from finite quantum ensembles. *Phys. Rev. Lett.* **74**, 1259–1263 (1995).
19. Bouwmeester, D. *et al.* Experimental quantum teleportation. *Nature* **390**, 575–579 (1997).
20. Ma, X.-S. *et al.* Quantum teleportation over 143 kilometres using active feed-forward. *Nature* **489**, 269–273 (2012).
21. Kim, Y. H., Kulik, S. P. & Shih, Y. Quantum teleportation of a polarization state with a complete Bell state measurement. *Phys. Rev. Lett.* **86**, 1370–1373 (2001).
22. Furusawa, A. *et al.* Unconditional quantum teleportation. *Science* **282**, 706–709 (1998).
23. Riebe, M. *et al.* Deterministic quantum teleportation with atoms. *Nature* **429**, 734–737 (2004).
24. Barrett, M. *et al.* Deterministic quantum teleportation of atomic qubits. *Nature* **429**, 737–739 (2004).
25. Olmschenk, S. *et al.* Quantum teleportation between distant matter qubits. *Science* **323**, 486–489 (2009).
26. Bao, X.-H. *et al.* Quantum teleportation between remote atomic-ensemble quantum memories. *Proc. Natl Acad. Sci. USA* **109**, 20347–20351 (2012).
27. Baur, M. *et al.* Benchmarking a quantum teleportation protocol in superconducting circuits using tomography and an entanglement witness. *Phys. Rev. Lett.* **108**, 040502 (2012).
28. Filipp, S. *et al.* Two-qubit state tomography using a joint dispersive readout. *Phys. Rev. Lett.* **102**, 200402 (2009).
29. Chuang, I. L. & Nielsen, M. A. Prescription for experimental determination of the dynamics of a quantum black box. *J. Mod. Opt.* **44**, 2455–2467 (1997).
30. Eichler, C. *et al.* Observation of two-mode squeezing in the microwave frequency domain. *Phys. Rev. Lett.* **107**, 113601 (2011).

Author Contributions The experiments were performed by L.S., A.F., Y.S., M.O., P.K. and M.B. The teleportation sample and parametric amplifiers were fabricated by A.F., L.S. and M.B. The air-bridge technology was developed by G.P.-H. and L.S. The FPGA firmware was implemented by Y.S. and C.L. The parametric amplifiers were designed by C.E., who also oversaw their operation. The manuscript was written by L.S., A.F. and A.W. All authors commented on the manuscript. The project was led by A.F. and A.W.

Author Information Reprints and permissions information is available at www.nature.com/reprints. The authors declare no competing financial interests. Readers are welcome to comment on the online version of the paper. Correspondence and requests for materials should be addressed to L.S. (lsteffen@phys.ethz.ch) or A.W. (andreas.wallraff@phys.ethz.ch).

METHODS

Sample parameters. The sample consists of three superconducting coplanar waveguide resonators and three qubits of the transmon type[31] as depicted in Fig. 2. The resonators R1 and R3 have bare resonance frequencies $\nu_r = \{7.657, 9.677\}$ GHz, respectively. They are coupled by gap and finger capacitors to their input and output lines. The overcoupled resonator decay rates are measured to be $\kappa/2\pi = \{2.4, 2.5\}$ MHz. The coupling capacitances are designed asymmetrically such that the decay rate through the input port is approximately 100-fold lower than through the output port. The resonator R2 is not coupled to any input or output line. Its resonance frequency is about 8.7 GHz and its decay rate is expected to be close to the internal decay rate[32]. From spectroscopic measurements we determine the maximum transition frequencies $\nu_{max} = \{6.273, 7.373, 8.390\}$ GHz and charging energies $E_C/h = \{0.297, 0.303, 0.287\}$ GHz of the qubits Q1, Q2 and Q3, respectively, where h is Planck's constant.

Qubits Q1 and Q2 are coupled to resonator R1 with coupling strengths $g/2\pi = \{0.260, 0.180\}$ GHz, and Q3 is coupled to resonator R3 with a coupling strength of $g/2\pi = 0.240$ GHz. The coupling of Q2 and Q3 to R2 is estimated from the transverse coupling strength (see below) to be $g/2\pi = 0.2$ GHz each.

For the presented experiments, the qubits were tuned to idle state transition frequencies $\nu = \{4.657, 5.390, 6.342\}$ GHz with miniature superconducting coils mounted underneath the chip[33]. At these frequencies we have determined their energy relaxation $T_1 = \{5.1, 3.1, 2.6\}$ μs and coherence times $T_2 = \{1.0, 1.1, 1.7\}$ μs.

Pulse scheme. All biased qubits and resonators are separated in frequency from each other by at least 750 MHz to suppress cross-talk.

The protocol (Fig. 1b) is implemented with the pulse scheme depicted in Extended Data Fig. 1. Single-qubit rotations are implemented by resonant Gaussian-shaped DRAG[34,35] microwave pulses 12 ns long with an average fidelity of more than 98% as determined by randomized benchmarking[36]. The controlled-PHASE gate is implemented by shifting the qubits with fast magnetic flux pulses to the avoided level crossing between the $|11\rangle$ and $|02\rangle$ states of the involved qubits[7,37]. The transverse coupling strengths of $J_{11,02}^{Q1,Q2}/2\pi = 12.2$ MHz (between qubits Q1 and Q2) and $J_{11,02}^{Q2,Q3}/2\pi = 10.4$ MHz (between Q2 and Q3) lead to pulse lengths for the CPHASE gates of $t = \{40.9, 47.9\}$ ns, respectively.

The Bell measurement (Extended Data Fig. 1, red elements) allows us to map any of the four Bell states to the $|00\rangle$ state by adding π-pulses to Q1 and Q2 to flip their states just before starting the measurement. Instead of applying these π-pulses directly, we change the phases of the preceding π/2-pulses accordingly, which can easily be verified to be equivalent.

Qubit readout. To realize single-shot measurements, the output signals of resonators R1 and R3 are amplified by dedicated Josephson parametric amplifiers[9,38]. The parametric amplifiers are similar to that used in ref. 30. They are realized as $\lambda/4$ coplanar waveguide resonators terminated by an array of 11 superconducting quantum interference devices (SQUIDs), which provide the necessary nonlinearity and make the operation frequencies tunable by miniature superconducting coils on the bottom of the sample holder[39]. The maximum frequencies for the two parametric amplifiers are $\nu_{max} = \{8.349, 10.141\}$ GHz for R1 and R3, respectively. To provide a fast response, large input capacitors were fabricated that resulted in a measured Josephson parametric amplifier line width of $\kappa/2\pi = \{334, 548\}$ MHz in the linear regime. For the experiments the parametric amplifiers were tuned to have a maximum gain of $G = \{20.4, 20.6\}$ dB with a 3-dB bandwidth of $B/2\pi = \{16, 85\}$ MHz at frequencies $\nu_{exp} = \{7.686, 9.737\}$ GHz.

For the experiments in which we post-selected on an individual Bell state, the transmission of R1 was measured at the readout frequency $\nu_{ro} = 7.686$ GHz, which is the mean value of the effective resonator frequencies for the qubits Q1 and Q2 in the state $|00\rangle$ and $|01\rangle$. The parametric amplifier is used in the phase-sensitive mode by tuning its transition frequency such that the maximum gain was achieved at the readout frequency ν_{ro} at which it was also pumped. Preparing the four computational basis states $|00\rangle$, $|01\rangle$, $|10\rangle$ and $|11\rangle$, applying a measurement tone to R1 and integrating the amplified transmission signal for 280 ns resulted in a distribution of the integrated measurement signals as shown in Extended Data Fig. 2a. We optimized for the readout contrast between the $|00\rangle$ and all other states. In this way, the mean values of the distributions of the integrated signals for the states $|00\rangle$, $|10\rangle$ (Extended Data Fig. 2a) have the largest separation. However, as a result of the finite qubit lifetime, some of the $|01\rangle$ and $|10\rangle$ states decay into the ground state and are visible in the data as such. We choose a threshold for the integrated quadrature values to discriminate 00 from all other measurement outcomes 01, 10 and 11 with a fidelity of $91.0 \pm 0.2\%$.

In the experiments in which we are able to distinguish between all four Bell states simultaneously, the readout frequency $\nu_{ro} = 7.683$ GHz is chosen to be the mean of the effective resonator frequencies for the qubits Q1 and Q2 in the state $|01\rangle$ and $|10\rangle$. The parametric amplifier is used in the phase-preserving mode by detuning the pump frequency by 6.25 MHz from the readout frequency. In this way the gain $G = 18.4$ dB at the readout frequency and the effective bandwidth are

smaller than for phase-sensitive amplification, but both quadratures of the transmitted field are amplified. By preparing the computational basis states and recording the integrated transmitted signals of both quadratures (I, Q) simultaneously, we can map every measurement outcome to a point on the complex plane. By adjusting the pump power and the readout power we find settings that maximize the distinguishability of all four states by their location in the complex plane.

Adjusting the phase of the local oscillator and implementing small linear offsets directly in the FPGA we are able to choose the $I = 0$ and $Q = 0$ axes of the complex plane as thresholds to identify the four different output states in real time (Extended Data Fig. 2b). By assigning our best estimate of the corresponding states to every measurement outcome according to a quadrant in the I–Q plane, we identify $(81.8 \pm 0.5)\%$ of the prepared states correctly. The probabilities of either correctly identifying a prepared state or misidentifying it as a different state are listed in Extended Data Table 1 for all four input basis states.

Feed-forward. To implement the feed-forward, all measurement data are analysed in real-time in an FPGA with custom firmware. Depending on the measurement outcome, the FPGA triggers up to two different arbitrary waveform generators (AWGs), which realize X and $\bar{Y}$ rotations. To optimize the readout fidelity and minimize the time needed for data analysis, we calibrate the phase of the down-conversion local oscillator to rotate the readout data of Q1 and Q2 such that the four different states can be distinguished by thresholds parallel to the I and Q axes of the complex plane. An additional small offset is subtracted digitally such that the assignment of a measured signal to a given state is based solely on the quadrant of the complex plane it lies in (see Extended Data Fig. 2b).

We integrate the signal for 160 ns to achieve the desired signal-to-noise ratio. This choice of integration time also digitally filters out the parametric amplifier pump tone, which is detuned by 6.25 MHz from the measurement tone. We experimentally determine a maximum readout fidelity by starting the integration time 140 ns after the initial rise of the pulsed measurement tone applied to the resonator. The FPGA used for data analysis and the AWG used for generating the feed-forward pulses introduce a combined delay of 140 ns; the total cable delay is 65 ns. As a result, the conditional rotations are applied to Q3 505 ns after the measurement tone has been applied to the readout resonator R1 (Extended Data Fig. 1). To mitigate dephasing of Q3 during this feed-forward delay time, we apply a series of four dynamical decoupling pulses to Q3.

We have also fully characterized the fidelity of the feed-forward process. After preparing the state indicated in the rows of Extended Data Table 2 and performing the conditional rotations indicated in the columns of Extended Data Table 2, the fidelity of the applied feed-forward process was determined. The diagonal elements indicate the fidelity of the desired feed-forward operations occurring with the probabilities shown in Extended Data Table 1. The off-diagonal elements indicate the fidelity of the unwanted rotations occurring with a smaller probability (Extended Data Table 1) but a similar fidelity.

Efficiency of the teleportation protocol. The total efficiency of the implemented teleportation protocol is close to unity. The main limitation is currently set by the heralding process of the initial ground state of all qubits. Before each individual experimental realization of the teleportation protocol, we apply a measurement tone 500 ns long to both resonators, to verify that all the qubits are in their ground states. This heralds the ground state with a total efficiency of more than 80% when using the parametric amplifiers in the phase-sensitive mode. In the phase-preserving mode we herald the ground state with ~65% probability while performing single-shot readout. This is in stark contrast to experiments in which optical photons are used as qubits, where the maximal reported efficiency is 0.1% (ref. 40). Using active initialization schemes for superconducting circuits[41–45], the efficiency of future experiments can probably be improved to approach 100% for sufficiently long qubit coherence times.

State and process tomography. To characterize the state transfer from Q1 to Q3 we performed full process tomography[29]. Performing state tomography on the output state $|\psi_{out}\rangle$ for four different input states $|\psi_{in}\rangle = |0\rangle, |1\rangle, (|0\rangle + |1\rangle)/\sqrt{2}$, $(|0\rangle - i|1\rangle)/\sqrt{2}$ (Extended Data Fig. 3), we obtain the process matrix χ through linear inversion. In state tomography we measure a state prepared repeatedly with a set of orthogonal measurement operators realized by applying either no pulse, a $\pi/2$-pulse about the x or y axis or a π-pulse to the qubit before measurement of its Z eigenstate.

Entanglement verification in a teleportation protocol. The initial shared two-qubit state was characterized by performing state tomography immediately after its generation, instead of continuing the teleportation protocol. The resulting Bell state has a fidelity of 92% and a concurrence of 0.89, demonstrating the entangled nature of the state. In addition it is also possible to use the teleportation protocol itself as method for entanglement verification[46]. If the average output-state fidelity for six mutually unbiased input basis states is above the classical threshold of 2/3, it unambiguously shows that the two parties shared an entangled state, even if one has no knowledge about the details of the protocol itself. We performed the

teleportation experiment with feed-forward also with the six mutually unbiased input basis states $|\psi_{in}\rangle = |0\rangle$, $|1\rangle$, $(|0\rangle + |1\rangle)/\sqrt{2}$, $(|0\rangle - i|1\rangle)/\sqrt{2}$, $(|0\rangle - |1\rangle)/\sqrt{2}$ and $(|0\rangle + i|1\rangle)/\sqrt{2}$ and found an average output-state fidelity $\tilde{\mathcal{F}}_s^{ff} = (69.3 \pm 0.1)\%$ with a process fidelity $\mathcal{F}_p^{ff} = (53.9 \pm 0.1)\%$.

Error budget. The finite coherence and dephasing times of our qubits are a source of error that limits the output-state fidelity. The fidelity of the measurement of Q3 through R3 affects the state fidelity of $|\psi_{out}\rangle$ directly. From the measured probabilities of correctly identifying the states $|0\rangle$ and $|1\rangle$ on Q3 we calculate the limit of the output-state fidelity through this source of error to be $\bar{\mathcal{F}}_s = 94\%$. In addition, the misidentification of the Bell states of Q1 and Q2 leads to an effective dephasing of $|\psi_{out}\rangle$. This limits the fidelity further to $\bar{\mathcal{F}}_s = 89\%$ and $\bar{\mathcal{F}}_s = 84\%$ for the respective cases in which we post-select on one Bell state only and in which we distinguish all Bell states with each measurement. Because both of these numbers are about 7–8% higher than the actually measured fidelities, it is plausible to assign the remaining errors to the limited gate fidelities. Determining the gate errors independently shows that we perform single-qubit operations with a fidelity greater than 98% and create Bell states with a fidelity of 92% using two-qubit CPHASE gates with a process fidelity of 90%.

31. Koch, J. *et al.* Charge-insensitive qubit design derived from the Cooper pair box. *Phys. Rev. A* **76,** 042319 (2007).
32. Göppl, M. *et al.* Coplanar waveguide resonators for circuit quantum electrodynamics. *J. Appl. Phys.* **104,** 113904 (2008).
33. Fink, J. M. *et al.* Dressed collective qubit states and the Tavis–Cummings model in circuit QED. *Phys. Rev. Lett.* **103,** 083601–083604 (2009).
34. Motzoi, F., Gambetta, J. M., Rebentrost, P. & Wilhelm, F. K. Simple pulses for elimination of leakage in weakly nonlinear qubits. *Phys. Rev. Lett.* **103,** 110501 (2009).
35. Gambetta, J. M., Motzoi, F., Merkel, S. T. & Wilhelm, F. K. Analytic control methods for high-fidelity unitary operations in a weakly nonlinear oscillator. *Phys. Rev. A* **83,** 012308 (2011).
36. Chow, J. M. *et al.* Randomized benchmarking and process tomography for gate errors in a solid-state qubit. *Phys. Rev. Lett.* **102,** 090502 (2009).
37. Strauch, F. W. *et al.* Quantum logic gates for coupled superconducting phase qubits. *Phys. Rev. Lett.* **91,** 167005 (2003).
38. Vijay, R., Slichter, D. H. & Siddiqi, I. Observation of quantum jumps in a superconducting artificial atom. *Phys. Rev. Lett.* **106,** 110502 (2011).
39. Eichler, C. & Wallraff, A. Controlling the dynamic range of a Josephson parametric amplifier. *arXiv:1305.6583* (2013).
40. Nölleke, C. *et al.* Efficient teleportation between remote single-atom quantum memories. *Phys. Rev. Lett.* **110,** 140403 (2013).
41. Ristè, D., van Leeuwen, J. G., Ku, H.-S., Lehnert, K. W. & DiCarlo, L. Initialization by measurement of a superconducting quantum bit circuit. *Phys. Rev. Lett.* **109,** 050507 (2012).
42. Ristè, D., Bultink, C. C., Lehnert, K. W. & DiCarlo, L. Feedback control of a solid-state qubit using high-fidelity projective measurement. *Phys. Rev. Lett.* **109,** 240502 (2012).
43. Murch, K. W. *et al.* Cavity-assisted quantum bath engineering. *Phys. Rev. Lett.* **109,** 183602 (2012).
44. Geerlings, K. *et al.* Demonstrating a driven reset protocol for a superconducting qubit. *Phys. Rev. Lett.* **110,** 120501 (2013).
45. Campagne-Ibarcq, P. *et al.* Persistent control of a superconducting qubit by stroboscopic measurement feedback. *Phys. Rev. X* **3,** 021008 (2013).
46. van Enk, S. J., Lütkenhaus, N. & Kimble, H. J. Experimental procedures for entanglement verification. *Phys. Rev. A* **75,** 052318 (2007).
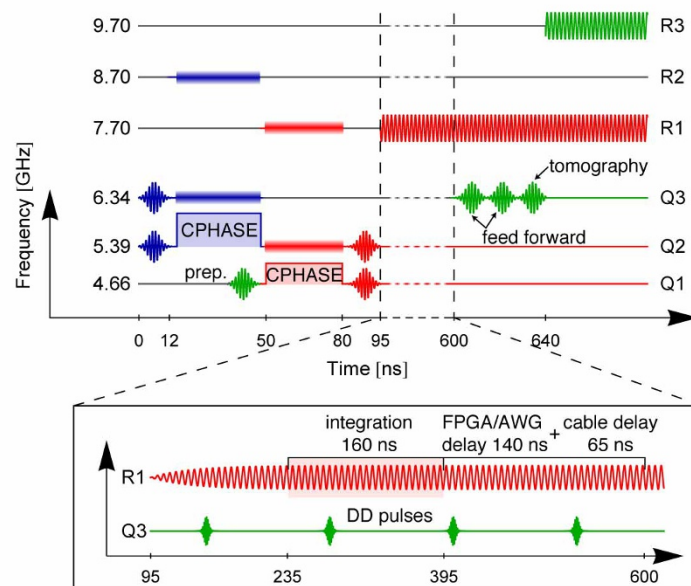
Extended Data Figure 1 | Pulse sequence of the teleportation protocol with feed-forward. The pulses implement the creation of an entangled pair between Q2 and Q3 (blue), the preparation of the state to be teleported on Q1 (green), the basis transformation from the Bell to the computational basis and the subsequent readout of Q1 and Q2 (red), the dynamical decoupling (DD) pulses, conditional rotations and the state tomography on Q3 (green). Gaussian-shaped sinusoids represent the microwave pulses applied to the respective charge bias lines of the qubits; sinusoids on the resonators represent the readout tones; and the squares labelled CPHASE represent the flux pulses that shift the frequency of a qubit to implement a controlled-PHASE gate between the marked qubits, where the interaction is mediated through the resonator indicated with a bar of the same colour as the flux pulse. The inset shows the time used for implementing the conditional feed-forward rotations. The total feed-forward time is the sum of the ramp-up time of the measurement tone, the integration time of the measurement signal and the delay times induced by the FPGA signal processing, the AWG trigger and the cables.
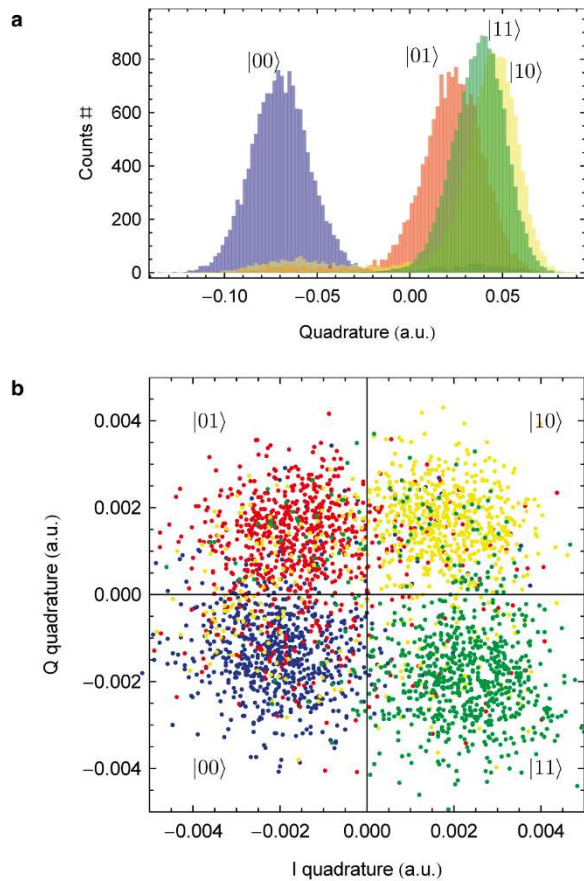
Extended Data Figure 2 | Characterization of the joint readout of Q1 and Q2. a, Histogram of the integrated signal quadrature-amplitude amplified phase-sensitively when preparing the states $|00\rangle$ (blue), $|01\rangle$ (red), $|10\rangle$ (yellow) and $|11\rangle$ (green). **b**, Scatter plot of integrated (I, Q) quadratures of the measurement signal amplified in the phase-preserving mode when preparing the states $|00\rangle$ (blue), $|01\rangle$ (red), $|10\rangle$ (yellow) and $|11\rangle$ (green).
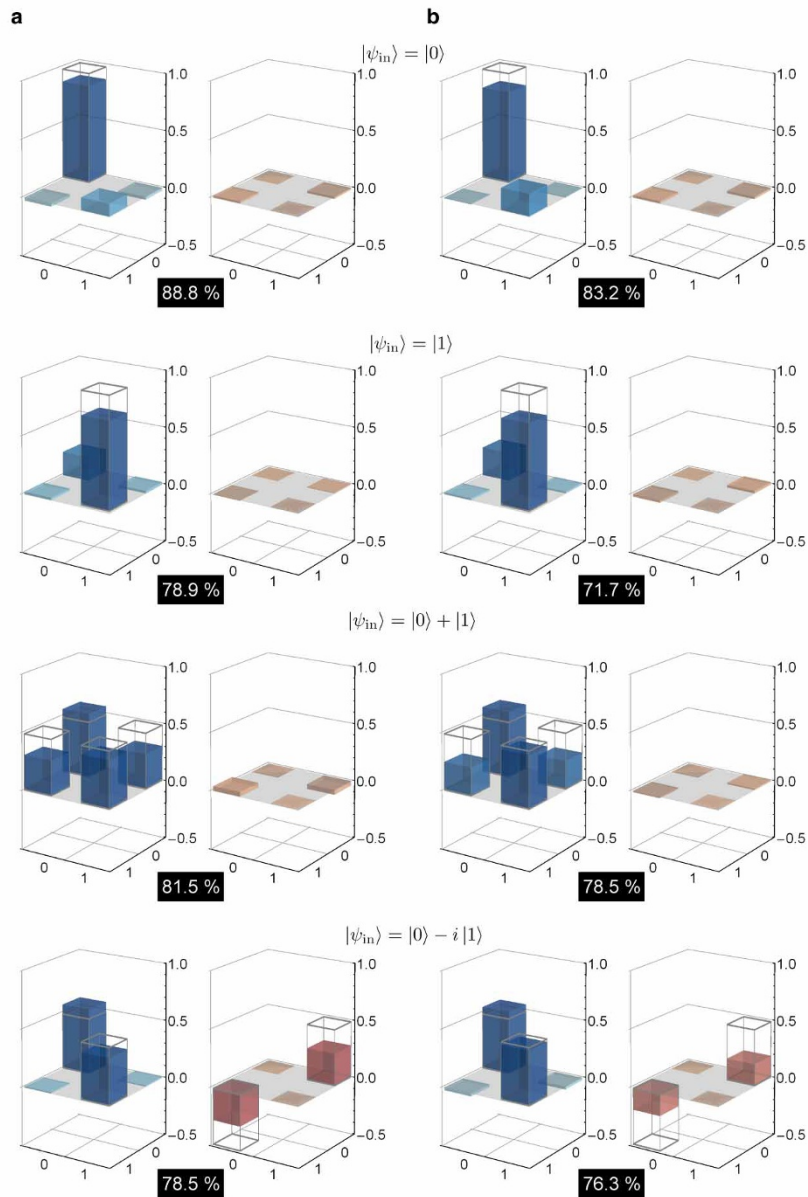
Extended Data Figure 3 | Characterization of the output states. Real (blue) and imaginary (red) parts of the reconstructed density matrices of the state $|\psi_{out}\rangle$ for the indicated input states $|\psi_{in}\rangle$ obtained from state tomography when (**a**) post-selecting data on a 00 outcome of the Bell measurement (**b**) using averaged readout on Q3 while performing fully deterministic teleportation with feed-forward. The ideally expected outcomes are indicated with wireframes. The state fidelities are indicated in the black boxes.

Extended Data Table 1 | Success probabilities for the joint readout

	00	01	10	11
$|00\rangle$	0.88	0.09	0.01	0.02
$|01\rangle$	0.11	0.79	0.08	0.02
$|10\rangle$	0.06	0.10	0.77	0.06
$|11\rangle$	0.02	0.03	0.08	0.87

Probabilities of identifying prepared input states (rows) as the indicated output state (columns). Correct identifications are diagonal elements; misidentifications are off-diagonal elements.

Extended Data Table 2 | Process fidelities of the feed-forward pulses

	I	X	Y	Z
$|00\rangle \otimes |\psi\rangle$	0.80	0.67	0.74	0.64
$|01\rangle \otimes X|\psi\rangle$	0.64	0.69	0.73	0.65
$|10\rangle \otimes Z|\psi\rangle$	0.66	0.63	0.66	0.65
$|11\rangle \otimes \tilde{Y}|\psi\rangle$	0.73	0.68	0.62	0.75

After preparing the indicated input states (rows) and performing the conditional operations (columns), the fidelity of the expected process is determined (elements of the table). The rows indicate the fidelity of the performed rotation conditioned on the measurement result of Q1 and Q2, which occur with the probabilities shown in Extended Data Table 1.